# Accurate Electronic and Optical Properties of Organic Doublet Radicals Using Machine Learned Range-Separated Functionals

Cheng-Wei Ju,[†,‡] Yili Shen,[¶,§] Ethan J. French,[†,‖] Jun Yi,[†] Hongshan Bi,[†] Aaron Tian,[†,⊥] and Zhou Lin[*,†]

†*Department of Chemistry, University of Massachusetts, Amherst, MA 01003, United States*

‡*Pritzker School of Molecular Engineering, The University of Chicago, Chicago, IL, 60637, United States*

¶*Manning College of Information and Computer Sciences, University of Massachusetts, Amherst, MA 01003, United States*

§*College of Software Engineering, Tongji University, Yangpu, Shanghai 200092, China*

‖*Department of Mathematics and Statistics, University of Massachusetts, Amherst, MA 01003, United States*

⊥*Massachusetts Academy of Math and Science, Worcester, MA, 01605, United States*

E-mail: zhoulin@umass.edu

**Abstract**

Luminescent organic semiconducting doublet-spin radicals are unique and emergent optical materials because their fluorescent quantum yields ($\Phi_{\text{fl}}$) are not compromised by spin-flipping intersystem crossing (ISC) into any dark high-spin states. The multi-configuration nature of these radicals challenges their electronic structure calculations in the framework of single-reference density functional theory (DFT) and introduces room for method improvement. In the present study, we extend our earlier development of ML-$\omega$PBE, a range-separated hybrid (RSH) exchange–correlation (XC) functional constructed using the stacked ensemble machine learning (SEML) algorithm, from closed-shell organic semiconducting molecules to doublet-spin organic semiconducting radicals. We assess its performance for a new test set of 64 radicals from five categories based on the original training set of 3,926 molecules. Interestingly, ML-$\omega$PBE agrees with the first-principles OT-$\omega$PBE functional regarding the molecule-dependent range-separation parameter ($\omega$), with a small mean absolute error (MAE) of 0.0197 $a_0^{-1}$ but saves the computational cost by 2.46 orders of magnitude. This result demonstrates outstanding domain adaptation capacity of ML-$\omega$PBE among various organic semiconducting species. To further assess the predictive power of ML-$\omega$PBE, we also compare its performance on absorption and fluorescence energies ($E_{\text{abs}}$ and $E_{\text{fl}}$) evaluated using time-dependent DFT (TDDFT) with nine conventional functionals. For most radicals, ML-$\omega$PBE reproduces experimental measurements of $E_{\text{abs}}$ and $E_{\text{fl}}$ with small MAEs of 0.222 and 0.121 eV, only marginally different from OT-$\omega$PBE. Our work illustrates a successful extension of the SEML framework from closed-shell molecules to open-shell radicals and will open the venue for calculating optical properties using single-reference TDDFT.

# 1 Introduction

An organic semiconducting doublet-spin radical can stabilize its unpaired electron through the delocalized $\pi$-conjugation and exhibit a non-conventional non-Aufbau configuration where the singly occupied molecular orbital (SOMO) is lower-lying than the highest (doubly) occupied molecular orbital (HOMO).[1–10] Such a long-lived open-shell configuration and the resulting compelling physicochemical characteristics, especially controllable optical properties between the doublet ground ($D_0$) and excited states ($D_{n\geq 1}$), make it promising functional material for emergent scientific fields. For example, in photothermal therapy (PTT), the radical anion like a supramolecular complex of benzodithiophene-fused perylene diimide (BPDI) and cucurbit[7]uril (CB[7]) absorbs biologically transparent near-infrared (NIR) light and dissipates the photon energy as heat.[11–15] In organic light-emitting diodes (OLEDs), the $D_1$ state can reach a 100% fluorescent quantum yield ($\Phi_{\text{fl}}$) because it does not undergo any easy intersystem crossing (ISC) into a high-spin dark state.[4,7,16–18]

The open-shell character of such an organic semiconducting radical makes its ground and excited state electronic structures challenging to calculate.[19] To address this problem while considering the molecular size, many multiconfigurational approaches have been developed on the foundations of density functional theory (DFT) and time-dependent density functional theory (TDDFT) and have been proven physically correct and reliable, including multiconfiguration pair DFT (MC-PDFT),[20–22] spin-adapted TDDFT (X-TDDFT),[23–26] spin-flip TDDFT (SF-TDDFT),[27–29] and orbital optimization DFT (OODFT).[30–32] However, the application of these multiconfigurational DFT approaches has been limitd to small and simple system because (1) it is difficult to select and handle appropriate active space and electronic configurations without prior knowledge of the system and (2) their typical computational costs of $\simeq N_{\text{act}}N_{\text{orb}}^4$ are less friendly for the typical size of an organic semiconducting radical.[33–35]

The low computational cost ($\simeq N_{\text{orb}}^3$) and the black-box character make regular single-reference DFT and TDDFT appealing again for organic semiconducting radicals despite the

above-mentioned theoretical challenge and the insufficient reliable benchmarks. DFT and TDDFT can generate ground and/or excited state electronic structures of these radicals to desired accuracy after careful development and calibration of the exchange–correlation (XC) functional.[23,24,36–43] Head-Gordon and coworkers performed systematic studies for excited state properties of polycyclic aromatic hydrocarbon (PAH) radical ions[38,44–48] using original linear response (LR) TDDFT and its simplified variant with Tamm–Dancoff approximation (TDA)[49] along with common functionals like BLYP[50,51] and B3LYP.[50–52] They found that TDDFT and TDDFT/TDA both reproduced experimental excited state energies with errors smaller than 0.3 eV when the basis set was reasonably large, in spite of the inexact XC functionals and adiabatic approximations and the inability to treat double excitations.[53,54] They also concluded that TDDFT/TDA outperformed TDDFT in capturing correct states by overcoming the orbital instability problem existing for some radicals.[49,55–59] They further assigned the strongest absorption of each radical to involve its SOMO.

Other researchers, such as Joblin,[39,60–62] Jacquemin,[41] Grimme,[63,64] Furche,[65–67] and Allouche,[68] performed similar benchmark analyses on organic semiconducting radicals using DFT and TDDFT and obtained physical insights and reaction mechanisms. All these DFT-based studies demonstrated the advantage of using a global hybrid functional, or a range-separated hybrid (RSH) functional[69–80] with molecule-dependent parameters for organic semiconducting radicals due to the necessity to balance the accuracy of electronic density between a semi-local XC functional like Heyd–Scuseria–Ernzerhof (HSE)[73] and Perdew–Burke–Ernzerhof (PBE)[81] and the Hartree-Fock (HF) exchange functional. the short and long ranges.

One outstanding example for a molecule-dependent RSH functional was developed by Kronik, Baer, and their coworkers based on the idea of optimal tuning (OT).[22,82–86] They utilized the range-separation parameter ($\omega$) which characterizes the inverse distance when the functional transitions from a semi-local formula in the short range to the HF formula in

the long range, appearing in the separation of the Coulomb operator

$$\frac{1}{|\mathbf{r}-\mathbf{r}'|} = \underbrace{\frac{1-\mathrm{erf}(\omega|\mathbf{r}-\mathbf{r}'|)}{|\mathbf{r}-\mathbf{r}'|}}_{\text{short range}} + \underbrace{\frac{\mathrm{erf}(\omega|\mathbf{r}-\mathbf{r}'|)}{|\mathbf{r}-\mathbf{r}'|}}_{\text{long range}} \tag{1}$$

They also optimized the value of $\omega$ based on Koopmans' theorem[87] by minimizing the metrics of

$$J^2(\omega) = [\varepsilon_{\mathrm{HOMO}}(\omega) + I(\omega)]^2 + [\varepsilon_{\mathrm{LUMO}}(\omega) + A(\omega)]^2 \tag{2}$$

However, this non-empirical, first-principles method is expensive for large organic semiconducting compounds because it can take twenty or more converged SCF calculations to determine a single value of $\omega$ without implementing the analytical gradient.

Motivated by the urgent demand for a more efficient approach of determining the molecule-dependent value of $\omega$, as well as the rapid advancement in state-of-the-art machine learning (ML) models, we designed a new RSH functional referred to as ML-$\omega$PBE.[80] Just like OT-$\omega$PBE, we utilized the same XC formula as LC-$\omega$PBE with an arbitrary value of $\omega$ and optimized the value of $\omega$ based on a stacked ensemble machine learning (SEML) algorithm[88–93] and a composite molecular descriptor (CMD).[94–99] We systematically trained and benchmarked ML-$\omega$PBE using 3,926 closed-shelled organic semiconducting molecules.[80,100–105]

Our comparison between the value of $\omega$ obtained from well-trained ML-$\omega$PBE ($\omega_{\mathrm{ML}}$) and its counterpart from OT-$\omega$PBE ($\omega_{\mathrm{OT}}$) reached an excellent agreement with a mean absolute error (MAE) as small as 2.5% of average $\omega_{\mathrm{OT}}$, but the computational cost of ML-$\omega$PBE was 99.8% lower than that of OT-$\omega$PBE. We also compared ML-$\omega$PBE-predicted optical properties with OT-$\omega$PBE and many popular functionals,[50–52,70,75,81,106–109] and found that ML-$\omega$PBE reproduced the accuracy of OT-$\omega$PBE and outperformed everyone else.

It is worth noticing that the test set in that study included some "external" molecules with *no* structural analogs present in the training set.[79,110–112] Their successful treatments indicate advantages of our SEML model and ML-$\omega$PBE functional that were seldom observed

in other ML models and XC functionals, referred to as a substantial capacity in transferability or *domain adaptation*.

In the present study, we will assess the capacity in domain adaptation for the SEML algorithm and the ML-$\omega$PBE functional from closed-shell organic semiconducting molecules to doublet-spin organic semiconducting radicals (Figures 1). We will achieve this goal through the benchmark of its predictive power in the optimal value of $\omega$ and the vertical absorption and fluorescence energies ($E_{\text{abs}}$ and $E_{\text{fl}}$) between $D_0$ and $D_1$ states. We will show that organic semiconducting radicals can adopt the success of ML-$\omega$PBE.

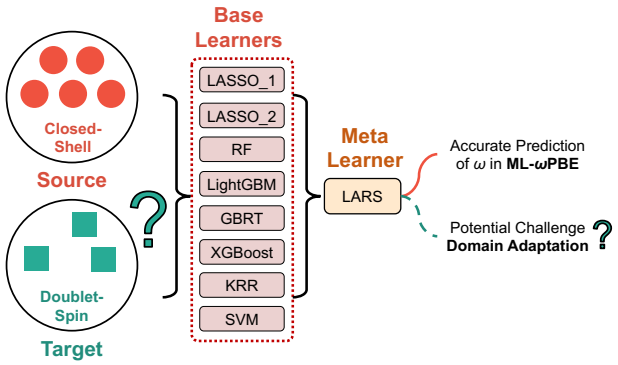


Figure 1: Architecture of the SEML model for ML-$\omega$PBE and potential challenge in domain adaptation from closed-shell molecules to doublet-spin radicals.

# 2 Methods

## 2.1 Training and Test Sets

Our training set combines the original training and test sets from the previous study,[80] and includes a total of 3,926 organic semiconducting molecules from six open-source and home-made datasets, including 1,941 from Harvard Clean Energy Project (CEP),[100,101] 904 from DeepChem,[102] 431 from ChemFluor,[103] 337 from Harvard Organic Photovoltaic 2015 (HOPV15),[104] 84 from uncompiled research of Aspuru-Guzik and co-workers,[105] and 229 from our own compilation.[80]

We also construct a brand new test set of 64 radicals, including 35 carbon-based radicals (C-1 through C-19 and C-49 through C-64),[17,113–133] 2 PAH-based radicals (PAH-20 and PAH-21),[134,135] 13 nitrogen-based radicals (N-22 through N-34),[136–144] 6 nitrogen-oxygen-based radicals (NO-35 through NO-40),[145–150] and 8 aryl oxygen-based radicals (ArO-41 through ArO-48).[151–158] In the Supporting Information (SI), we provide the Cartesian (XYZ) coordinates associated with optimized geometries of these radicals for $D_0$ and $D_1$ states, as well as their experimental measurements of $E_{\text{abs}}$ or $E_{\text{fl}}$ and optimal values of $\omega_{\text{OT}}$ and $\omega_{\text{ML}}$.

In the following sections, we will show that the absence of radical species from the training set does not undermine the predictive power of ML-$\omega$PBE in $\omega$, electronic structures, and optical properties.

## 2.2 Molecular Descriptor

To represent the structural and electronic configurations for all species in the training and test sets, we construct a CMD following the same procedure as the previous study.[80] This CMD is a vector that collects information from a few inexpensive molecular properties, including combined molecular fingerprints (CMFs),[94–96] physical organic descriptors (PODs),[94] and semi-empirical electronic structure properties (ESPs) from tight-binding method GFN2-xTB developed by Grimme and coworkers.[97–99] This tight-binding calculation turns out to be the rate-determining step for the construction of the CMD and the determination of $\omega_{\text{ML}}$ from the well-trained ML-$\omega$PBE.

## 2.3 Stacked Ensemble Machine Learning

Our "top-down" SEML algorithm, as described in detail in Figure S1 and Algorithm S1 in SI, implements the stacked generalization of eight successful descriptor-based regression models (or base learners), including least absolute shrinkage and selection operator (LASSO_1 and LASSO_2, differing in molecular descriptors),[159] random forest (RF),[160] gradient boosted regression trees (GBRT),[161] eXtreme Gradient Boosting (XgBoost),[162] light gradient boost-

ing machine (LightGBM),[163] kernel ridge regression (KRR),[164] and support vector machine (SVM).[165] We select these regression models as base learners rather than the more popular neural networks (NNs) because they are less expensive, less data-demanding, and interestingly, more powerful when the sizes of molecules and datasets are larger.[166–173] Each base learner generates a non-linear quantitative relationship between the CMD and the optimal $\omega_{\mathrm{ML}}$.

We also use the least angle regression (LARS)[174] method as the meta learner to collect and analyze above-mentioned quantitative relationships from all base learners and provide the final prediction of $\omega_{\mathrm{ML}}$. Earlier studies demonstrated that stacked generalization is more powerful and accurate than every single regression model among base learners.[80,88–93]

The source code and database associated with the present study has been uploaded to the GitHub repository of the Lin Group.[175]

## 2.4 Computational Details

All first-principles electronic structure calculations in the present study, including those using DFT, TDDFT, complete active space self-consistent field (CASSCF), and complete active space configuration interaction (CASCI), are performed using the developmental version of the Q-Chem 5.4 package.[176] The semi-empirical tight-binding calculations as part of CMDs are performed in GFN2-xTB.[97–99] The initial guess of any radical geometry is generated based on its simplified molecular-input line-entry system (SMILES) using RDKit.[177] Its $D_0$ geometry is optimized using ground state DFT[178,179] at the level of PBE0[106,107]/6-31G(d), and its $D_1$ geometry is optimized using TDDFT[180–182] at the level of CAM-B3LYP[108]/6-31G(d). The values of $\omega_{\mathrm{OT}}$ are optimized using the golden section search algorithm,[183] and those of $\omega_{\mathrm{ML}}$ are generated directly using the SEML model.

Based on the values of $\omega_{\mathrm{ML}}$ and the correct geometries, $E_{\mathrm{abs}}$ and $E_{\mathrm{fl}}$ are calculated using TDDFT and TDDFT/TDA,[49] the basis sets of 6-311G(d) and 6-311G+(d), and the

equations

$$E_{\text{abs}} = E(\text{D}_1|\text{D}_0) - E(\text{D}_0|\text{D}_0) \tag{3}$$

$$E_{\text{fl}} = E(\text{D}_1|\text{D}_1) - E(\text{D}_0|\text{D}_1) \tag{4}$$

These energies are compared with those generated by OT-$\omega$PBE as well as eight conventional functionals in the assessment, including LC-$\omega$PBE ($\omega = 0.200$ and $0.300\ a_0^{-1}$),[75,76] PBE,[81] PBE0,[106,107] B3LYP,[50–52] CAM-B3LYP ($\omega = 0.330\ a_0^{-1}$),[108] M06-2X,[109] and $\omega$B97X-D3 ($\omega = 0.250\ a_0^{-1}$).[70]

The polarizable continuum model (PCM)[184] is used to represent the solvation effect for the singlet point calculations of $E_{\text{abs}}$ and $E_{\text{fl}}$. The dielectric constant ($\epsilon$) used for each species agree with the solvents used in corresponding experimental measurements.[17,113–116,118–143,145–158]

# 3 Results

## 3.1 Domain Adaptation

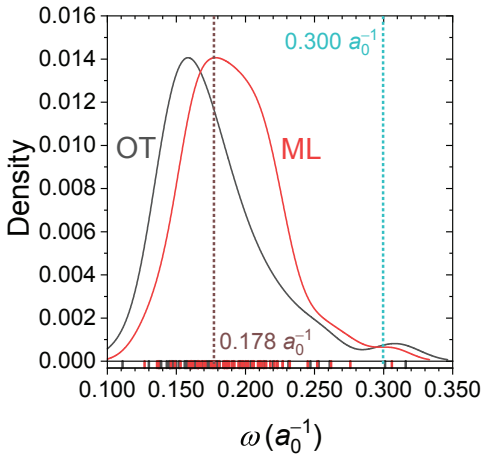


Figure 2: Distributions of $\omega_{\text{ML}}$ and $\omega_{\text{OT}}$ ($a_0^{-1}$) for all radicals from the test set, with the average $\langle\omega_{\text{OT}}\rangle = 0.178\ a_0^{-1}$ and the popular $\omega = 0.300\ a_0^{-1}$ labeled.

In the present section, we evaluate the performance of ML-$\omega$PBE from a few different

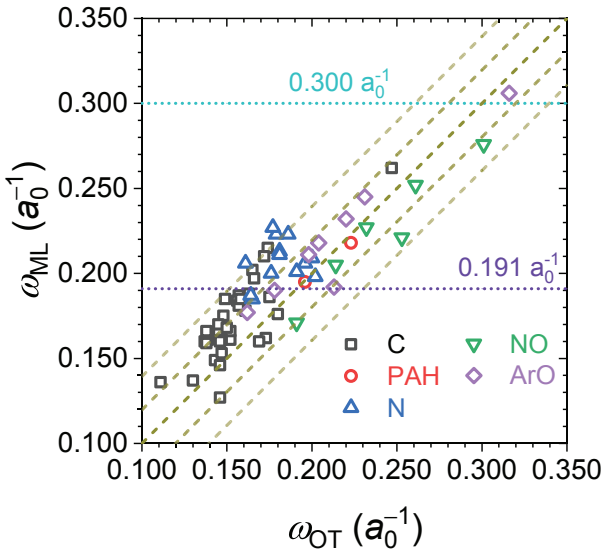


Figure 3: Comparison between $\omega_{\mathrm{ML}}$ and $\omega_{\mathrm{OT}}$ for all radicals from the test set, with the average $\langle\omega_{\mathrm{ML}}\rangle = 0.191\ a_0^{-1}$ and the default $\omega = 0.300\ a_0^{-1}$ labeled, as well as $\omega_{\mathrm{ML}} - \omega_{\mathrm{OT}} = 0, \pm\Delta\omega, \pm 2\Delta\omega$.

aspects, but we place the top priority on its potential in domain adaptation. We will confirm a high capacity of ML-$\omega$PBE in domain adaptation by showing that the non-linear quantitative relationship between the CMD and $\omega_{\mathrm{ML}}$ can be extrapolated from the domain of closed-shell organic semiconducting molecules to that of doublet-spin organic semiconducting radicals.

Figure 2 shows wide distributions of $\omega_{\mathrm{OT}}$ and $\omega_{\mathrm{ML}}$ between 0.120 and 0.320 $a_0^{-1}$, as generated for the entire test set of radicals. This result is similar to the training set[80] and indicates the necessity to implement a molecule-dependent value of $\omega$ for any organic semiconducting radical rather than selecting a universal value, if reliable electronic structures are needed. For example, the typical choice of $\omega = 0.300\ a_0^{-1}$ from LC-$\omega$PBE[75] is doom to fail to describe our radicals because the majority of $\omega_{\mathrm{ML}}$ and $\omega_{\mathrm{OT}}$ are far from 0.300 $a_0^{-1}$. In addition, the average value $\langle\omega_{\mathrm{OT}}\rangle = 0.178\ a_0^{-1}$ is significantly lower than the training set ($\langle\omega_{\mathrm{OT}}\rangle = 0.206\ a_0^{-1}$), suggesting that doublet-spin radicals exhibit an overall shift of the distribution to the lower end because their electronic structures are more diffuse and delocalized.

Figure 3 compares the values of $\omega_{\mathrm{ML}}$ and $\omega_{\mathrm{OT}}$ for all radicals from the test set and illus-

trates an excellent agreement between each other with a small MAE of $\langle \Delta_{\mathrm{ML}} \rangle = 0.0197\ a_0^{-1}$ and a narrow distribution of deviations. The absolute error (AE) for 33 out of the 64 radicals is smaller than MAE ($\Delta_{\mathrm{ML}} \leq \langle \Delta_{\mathrm{ML}} \rangle$) and that for the other 27 is smaller than twice the MAE ($\Delta_{\mathrm{ML}} \leq 2\,\langle \Delta_{\mathrm{ML}} \rangle$). Compared to the previous study on closed-shell molecules,[80] the current MAE for doublet-spin radicals is more than three times as large. However, we can still claim the successful domain adaptation of ML-$\omega$PBE because (1) this value is only 11.1% of $\langle \omega_{\mathrm{OT}} \rangle$ and 10.3% of $\langle \omega_{\mathrm{ML}} \rangle$ and turns out not to affect the predictive power of ML-$\omega$PBE and (2) there are only molecules but *no* radicals in the current training set. Regarding the computational complexity, ML-$\omega$PBE spends an average of 221 seconds to generate $\omega_{\mathrm{ML}}$ for each radical while OT-$\omega$PBE requires an average of 63,442 seconds to evaluate $\omega_{\mathrm{OT}}$, arriving a substantial save of 99.7%. This result proves that ML-$\omega$PBE is as successful for radicals as for molecules, with a comparable accuracy to OT-$\omega$PBE in $\omega$ but a considerably higher efficiency.

## 3.2 Chemical Space

To explore the origin behind the successful domain adaptation of ML-$\omega$PBE, we visualize the high-dimensional CMD and analyze the chemical space occupied by the training and test sets by illustrating the t-distributed stochastic neighbor embedding (t-SNE)[187] with an embedded space of two. To extract important molecular representation features and validate the advantage of a CMD, we compare the performance of a simplified CMD constructed using ECFP4 (Morgan)[95,185] and PaDEL[186] fingerprints (Figure 4(a)), and the simple ECFP4 fingerprint (Figure 4(b)). Our t-SNE results demonstrate obviously that the features of radicals in the test set are highly diversified as long as the chemical space is described using an appropriate CMD, but their range significantly overlap with molecules from the training set. This observation partially deciphers the cause of a successful domain adaptation. Also, compared to the simple ECFP4 fingerprint, the t-distribution given by the simplified CMD from ECFP4 and PaDEL fingerprints shows a more substantial although not perfect natural

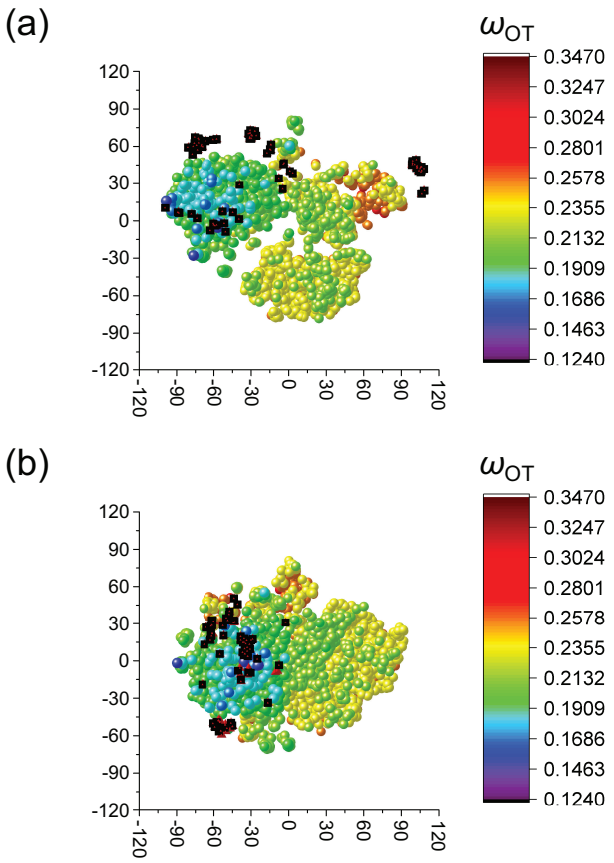


Figure 4: t-SNE results on all molecules from the training set (colorful spheres) and all radicals from the test set (black cubes) along with their hydrogenated counterparts (red tetrahedrons) are described using the CMD from (a) ECFP4 (Morgan)[95,185] and PaDEL[186] fingerprints and (b) the simple ECFP4 fingerprint. The color bar represents the scale of $\omega_{OT}$.

clustering, validating a stronger capacity of CMD in differentiating species and indicating a room for improvement in molecular representations.[188–192]

As a further validation of the overlap in chemical space between the training and test sets, Figure 5 compares the value of $\omega_{ML}$ for all radicals in the test set to their closed-shell hydrogenated counterparts (with an additional hydrogen atom attached to the radical site), and shows that they are very close to each other with a tiny MAE of 0.00434 $a_0^{-1}$. Most of the large deviations are caused by significant changes in semi-empirical electronic structures after the additional hydrogen atom is introduced such as C-4 and C-6. The chlorine atom near

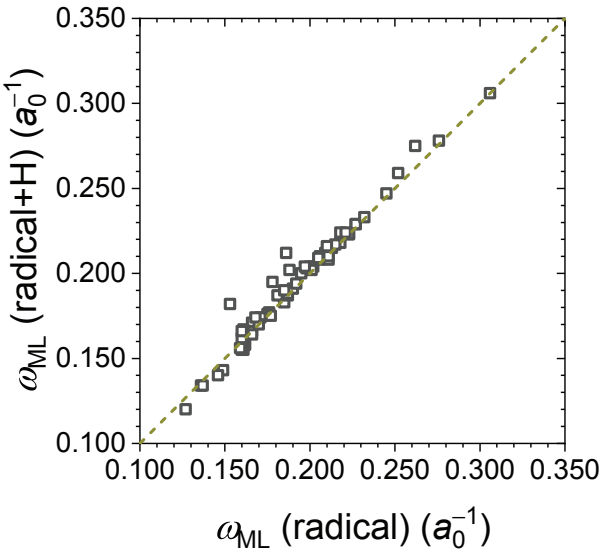


Figure 5: Comparison in $\omega_{\mathrm{ML}}$ between all radicals from the test set and their hydrogenated counterparts.

the radical site might help stabilize the unpaired electron through hyperconjugation, which might be undermined by adding hydrogen atom. Figures S3 through S7 compares frontier molecular orbitals (MOs) obtained from ML-$\omega$PBE for five representative radicals from the test set, including C-4, C-6, C-7, C-13, and N-23, and their hydrogenated counterparts. The extreme similarity between each other proves that the molecular features extracted by our CMD and SEML model are so stable that similar electronic structures lead to similar predictions of $\omega_{\mathrm{ML}}$.

## 3.3 Choice of Range Separation Parameters

Before we systematically discuss the accuracy of ML-$\omega$PBE on radical electronic structures, we will take a short detour and examine the sensitivity of electronic structures to the choice of $\omega$ using the formula of LC-$\omega$PBE, as motivated by the insufficient benchmark of RSH functionals on open-shell systems. To facilitate this discussion we select two representative molecules from the training set, including AIE-16 with a locally excited (LE) singlet first excited state ($S_1$)[80,110] and TADF-8 with a charge transfer (CT) $S_1$ state,[80,112] as well as three representative radicals from the test set, including C-6 with a primarily CT $D_1$ state,

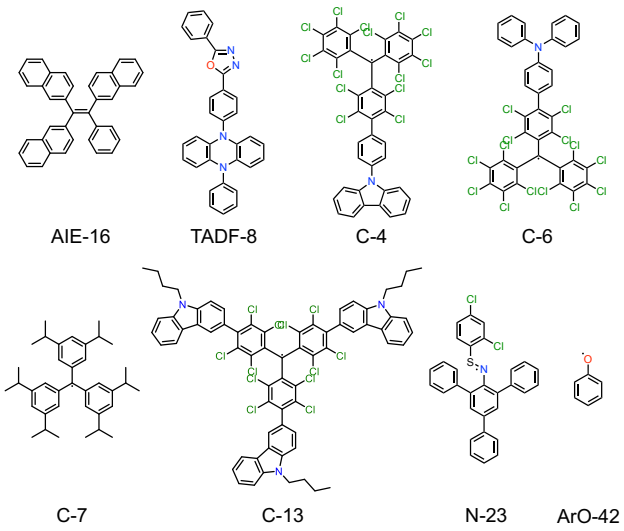


Figure 6: Structures of 2,2',2"-(2-phenylethene-1,1,2-triyl)trinaphthalene (AIE-16), 2-phenyl-5-(4-(10-phenylphenazin-5(10H)-yl)phenyl)-1,3,4-oxadiazole (TADF-8), 4'-(9H-carbazol-9-yl)-2,3,5,6-tetrachloro-[1,1'-biphenyl]-(bis(perchlorophenyl)methyl (C-4), (2',3',5',6'-tetrafluoro-N,N-diphenyl-4-amine-[1,1'-biphenyl])-(bis(perchlorophenyl))methyl (C-6), tris(3,5-diisopropylphenyl)methyl (C-7), tris(4-(9-butyl-9H-carbazol-3-yl)-2,3,5,6-tetrachlorophenyl)methyl (C-13), S-(2,4-dichlorophenyl)-N-(5'-phenyl-[1,1':3',1"-terphenyl]-2'-yl)thiohydroxylaminyl (N-23), and phenoxy (ArO-42).

C-7 with a primarily LE $D_1$ state, and N-23 with a partial CT $D_1$ character (Figure 6).

Figures 7 and S2 illustrate the configurations of frontier MOs for $\alpha$ and $\beta$ electrons associated with C-6, C-7, and N-23. They are all evaluated using LC-$\omega$PBE as functions of $\omega$ between 0.050 and 0.400 $a_0^{-1}$. Figures S10 through S17 provide natural transition orbital (NTO) pairs associated with their $D_0 \rightarrow D_1$ transitions. In our calculations, the unpaired electron is always set to $\alpha$, so that the change in the orbital configuration from $\beta$ to $\alpha$ electrons demonstrates the change in the electronic structures before and after introducing the unpaired electron.

In addition to a universal significant energy decrease from an unoccupied SOMO to its occupied counterpart, C-6 and N-23 also exhibit re-ordered energies and/or mixed characters for their SOMO, HOMO, and/or HOMO$-1$, or in other words *non-Aufbau* configurations, after involving the unpaired electrons. For both radicals, the $\beta$ HOMO $\rightarrow$ SOMO transition dominates the $D_0 \rightarrow D_1$ transition because the $\beta$ HOMO–SOMO energy gap is smaller

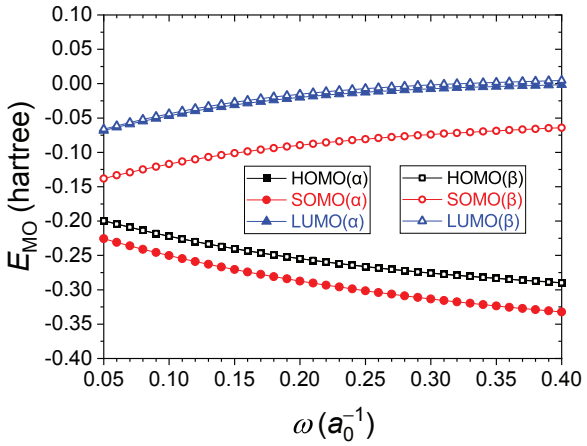


Figure 7: Energies of frontier MOs (hartree) for C-6 as functions of $\omega$ ($a_0^{-1}$) using LC-$\omega$PBE.

than the $\alpha$ SOMO–LUMO gaps. Limited spatial overlaps between MO and NTO pairs validate their CT and partial-CT characters. C-7, on the other hand, maintains its Aufbau configuration, but its $D_0 \rightarrow D_1$ transition gives a mixed transition of $\alpha$ SOMO $\rightarrow$ LUMO and $\beta$ HOMO $\rightarrow$ SOMO because of similar energy gaps. Significant spatial overlap between MOs and NTO pairs confirms its LE character. These results endorse the possibility of vital change in orbital configuration when their occupations vary.

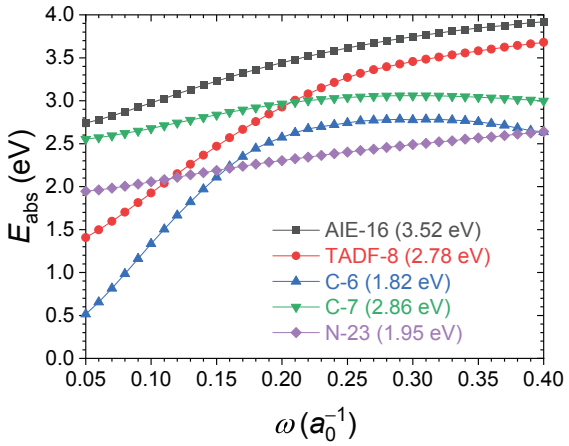


Figure 8: Calculated $E_{\text{abs}}$ (eV) as functions of $\omega$ ($a_0^{-1}$) using LC-$\omega$PBE, with experimental $E_{\text{abs}}$ in the parentheses.

Figure 8 exhibits the evaluated values of $E_{\text{abs}}$ as functions of $\omega$ for all five species, and presents bimodal relationships. For AIE-16, TADF-8, and N-23, $E_{\text{abs}}$ monotonically increases

with $\omega$ as expected, because the raised effective fraction of HF exchange over-localizes electrons and over-estimates $E_{\text{abs}}$.[193] Their leading NTO pairs (Figures S8, S9, and S17) remain similar across the broad range of $\omega$, except that the fraction of the CT character monotonically decreases with an increasing $\omega$, and small contributions (amplitude $< 0.20$) from other transitions might appear. On the contrary, C-6 and C-7 demonstrate non-monotonic trends in $E_{\text{abs}}$. They increase first with the rising $\omega$, peak at $\omega = 0.310$ and $0.290$ $a_0^{-1}$, respectively, and decrease afterward. In addition to the ever-increasing localization of MOs, their NTO pairs (Figures S10 through S16) also shift characters and become are more complicated between 0.200 and 0.300 $a_0^{-1}$.

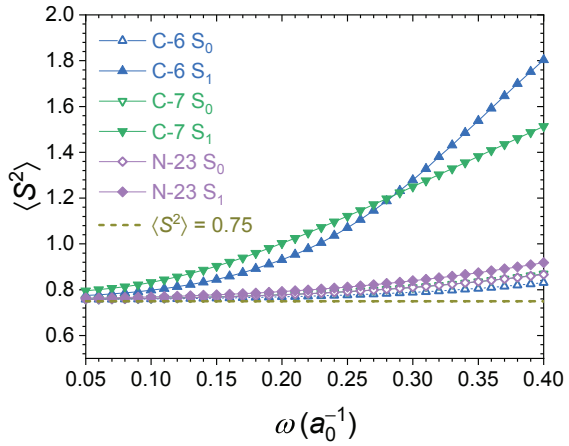


Figure 9: Calculated $\langle S^2 \rangle$ associated with $D_0$ and $D_1$ as functions of $\omega$ ($a_0^{-1}$) using LC-$\omega$PBE, with $\langle S^2 \rangle = 0.75$ labeled for a pure doublet state.

Figure 9 presents the total spin configuration ($\langle S^2 \rangle$) associated with $D_0$ and $D_1$ states for C-6, C-7, and N-23, and further rationalize the mixing of NTOs. Although all radicals in question present a universal increasing spin symmetry breakdown with an increasing fraction of HF exchange, neither $D_0$ nor $D_1$ state of N-23 experiences a significant shift from an expected pure doublet ($\langle S^2 \rangle = 0.75$), while $D_1$ states of C-6 and C-7 experience more substantial mixing from quartets ($\langle S^2 \rangle = 3.75$) or higher spin states compared to $D_0$. The notable breakdown of C-6 and C-7 agrees with the ever-increasing mixing character of NTO pairs and explains bimodal configurations for $E_{\text{abs}}$. The situation is exceptionally serious for

C-6 because its NTO pairs are more delocalized and charge transferred.

All discussions herein and later reveal an important reason for optimizing $\omega$ for organic semiconducting radicals. This is because difficulty and instability are embedded in RSH functionals when applied to open-shell systems, making the subtle balance between over-delocalizing PBE and over-localizing HF important. In particular, the excited-state electronic structures of doublet-spin radicals are susceptible to the choice of $\omega$, especially when they exhibit more delocalized or CT characters.

## 3.4 Optical Properties

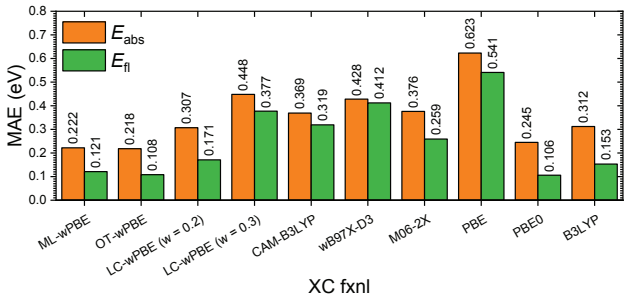


Figure 10: MAEs (eV) of $E_{\text{abs}}$ and $E_{\text{fl}}$ evaluated using ML-$\omega$PBE and TDDFT/6-311G(d) for relevant radicals from the test set and compared with eight conventional XC functionals.

We will benchmark ML-$\omega$PBE by examining its predictive power for $E_{\text{abs}}$ and $E_{\text{fl}}$ of doublet-spin radicals in the test set. We construct the test subset for $E_{\text{fl}}$ using C-49 through C-64 and the test subset of $E_{\text{abs}}$ using the rest of the radicals. We calculate $E_{\text{abs}}$ and $E_{\text{fl}}$ for relevant radicals using ML-$\omega$PBE and different basis sets in the framework of LR TDDFT and TDDFT/TDA and compare their accuracy in terms of MAEs and/or mean signed errors (MSEs) with OT-$\omega$PBE[79,80] and seven other popular XC functionals as described in computational details.[50–52,70,75,76,81,106–109] We provide all statistics in Figure 10 and Tables S1 through S7 in the SI and draw a few conclusions about the outstanding performance of ML-$\omega$PBE from these results.

To begin with, we re-validate the above-mentioned high sensitivity of the accuracy of $E_{\text{abs}}$ and $E_{\text{fl}}$ to the choice of $\omega$, especially for radicals with CT-like $D_1$ states like C-6. As

expected earlier, the standard LC-$\omega$PBE with $\omega = 0.300\ a_0^{-1}$ shows a poor performance regardless of the choice of the TDDFT variant and the basis set, because $0.300\ a_0^{-1}$ is significantly larger than $\omega_{\mathrm{ML}}$ for all radicals except for the smallest ArO-42 (Figure 6). On the other hand, if we reduce $\omega$ to a value closer to $\langle\omega_{\mathrm{OT}}\rangle = 0.178\ a_0^{-1}$ and $\langle\omega_{\mathrm{ML}}\rangle = 0.191\ a_0^{-1}$, like $\omega = 0.200\ a_0^{-1}$, LC-$\omega$PBE improves its performance but does not reach consistently comparable MAEs and MSEs with ML-$\omega$PBE and OT-$\omega$PBE because its value of $\omega$ is fixed. This situation is particularly serious for large carbon-based radicals with significantly lower values of $\omega$, such as C-4 ($\omega_{\mathrm{ML}} = 0.162\ a_0^{-1}$) and C-13 ($\omega_{\mathrm{ML}} = 0.137\ a_0^{-1}$). The re-validated sensitivity re-emphasizes the necessity to apply a molecule-dependent $\omega$ to organic semiconducting radicals.

Next we will show that well-trained ML-$\omega$PBE outperforms conventional functionals and accurately reproduces experimental optical properties. For the carbon-, PAH-, nitrogen, and nitrogen-oxide-based radicals in the $E_{\mathrm{abs}}$ test subset, ML-$\omega$PBE illustrates a distinct performance with an overall MAE of 0.222 eV and an overall MSE of +0.126 eV using TDDFT/6-311G(d), being only marginally different from OT-$\omega$PBE and exceeding all other functionals. A similar behavior is observed for carbon-based radicals in the $E_{\mathrm{fl}}$ test subset. We attribute these achievements to the excellent agreement between $\omega_{\mathrm{ML}}$ and $\omega_{\mathrm{OT}}$ (Figure 3), as well as the detailed balance between PBE and HF and between LE and CT, for most of the radicals in question. Further, this result re-implies the robustness of ML-$\omega$PBE among distinct domains. In particular our CMD can precisely represent the features of these radicals and the SEML algorithm can reliably construct a quantitative relationship between the CMD and $\omega_{\mathrm{ML}}$.

To visualize our analysis, we compare the characters of frontier $\alpha$ MOs using C-4 as an example. Figure 11(a) gives the energy ordering of HOMO$-1$ < SOMO < HOMO predicted by the *ab initio* CASCI (14,11) approach, as well as frontier $\alpha$ MOs that bear the same characters of the three from all functionals in question. ML-$\omega$PBE ($\omega = 0.162\ a_0^{-1}$), OT-$\omega$PBE ($\omega = 0.173\ a_0^{-1}$), and LC-$\omega$PBE ($\omega = 0.200\ a_0^{-1}$) slightly switch this order by giving

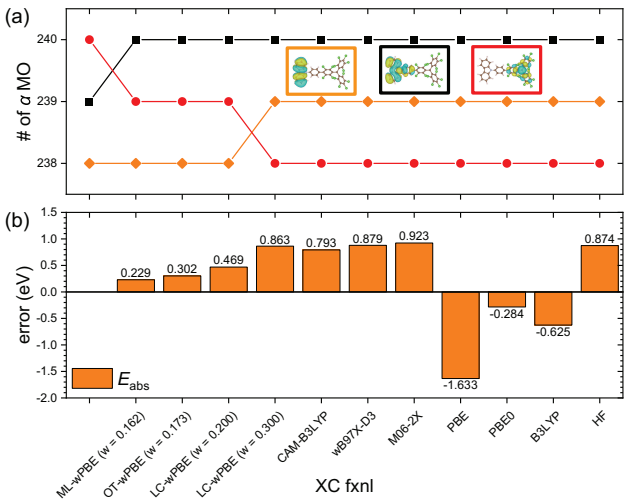


Figure 11: (a) Numbering of frontier $\alpha$ MOs of C-4 that bear the leading characters of HOMO$-$1 (orange), HOMO (black), and SOMO (red) from the benchmark CASCI (14,11) calculation, evaluated using various XC functionals. (b) SEs (eV) for $E_{\text{abs}}$ of C-4 evaluated using various XC functionals.

HOMO$-$1 $<$ SOMO $<$ HOMO, while all other functionals considerably shuffle this order by giving SOMO $<$ HOMO$-$1 $<$ HOMO. Figure 11(b) gives the signed errors (SEs) of $E_{\text{abs}}$ obtained from all these functionals, and shows that the general errors of ML-$\omega$PBE, OT-$\omega$PBE and LC-$\omega$PBE ($\omega = 0.200\ a_0^{-1}$) are significantly smaller than other functionals, agreeing with the trend of the energy orders. This result justifies the importance of obtaining correct key electronic structures in predicting optical properties.

Among the non-RSH functionals in comparison, the global hybrid PBE0[106,107] with 75% PBE[81] and 25% HF appears to be an exception because it occasionally gives smaller MAEs and MSEs than ML-$\omega$PBE and OT-$\omega$PBE. This behavior is highly likely due to the error cancellation between $D_0$ and $D_1$. However, considering the re-ordered frontier MOs of C-4 reported by PBE0 (Figure 11(a)) , we conclude that a great energy agreement does not necessarily equal a great description of electronic structures.

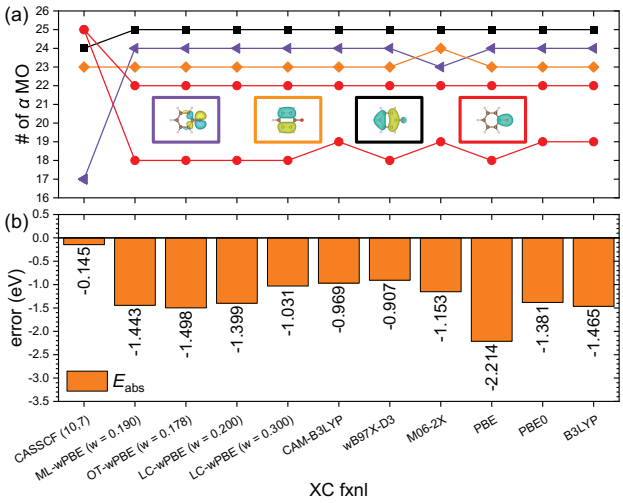


Figure 12: (a) Numbering of frontier $\alpha$ MOs for ArO-42 that bear the leading characters of HOMO$-$7 (green), HOMO$-$1 (orange), HOMO (black), and SOMO (red) from the benchmark CASSCF (10,7) calculation, evaluated using various XC functionals. (d) SEs (eV) for $E_{\text{abs}}$ of ArO-42 evaluated using various XC functionals.

## 3.5 Aryl Oxygen Radicals

Any aryl oxygen-based radical from the test set underestimates the value of $E_{\text{abs}}$ by more than 1 eV regardless of the choice of the functional. We will show that this huge error originates from the incorrect or unstable electronic structures obtained from single-reference DFT and TDDFT. To showcase our idea, we select ArO-42, the smallest aryl oxygen-based radical and calculate its $E_{\text{abs}}$ and four frontier MOs (HOMO$-$7, HOMO$-$1, HOMO, and SOMO) using ML-$\omega$PBE, all other functionals in the discussion, and *ab initio* CASSCF and CASCI approaches (Figure 12).

Based on our analysis, the errors of $E_{\text{abs}}$ obtained from all DFT methods are significantly greater than the benchmark CASSCF (10,7) calculation ($-0.145$ eV) due to the substantially re-ordered frontier MOs. For example, SOMO (# 25) predicted by CASSCF (10,7) represents a localized $\pi_z$ bond between the oxygen atom and the carbon atom next to it. However, this orbital is split into HOMO$-$6 (# 18) and HOMO$-$2 (# 22) by ML-$\omega$PBE ($\omega = 0.190\ a_0^{-1}$) and OT-$\omega$PBE ($\omega = 0.178\ a_0^{-1}$). On the other hand, SOMO predicted by ML-$\omega$PBE and OT-$\omega$PBE represents a delocalized $\pi_y^*$ bond at the same position but is originally HOMO$-$7

(# 17) from CASSCF (10,7). Frontier MOs from all of the rest functionals exhibit similar re-ordered behaviors. These results illustrate a fundamental problem in single-reference DFT, which can introduce serious errors to radicals with a highly localized unpaired electron, even after the most careful calibration of the XC functional. Herein we also re-confirm the essence of obtaining correct electronic structures.

### 3.6 TDDFT Variants and Basis Sets

We compare the performance of ML-$\omega$PBE across different combinations of TDDFT variants and basis sets. The basis set with diffuse functions, 6-311G+(d), does not improve the accuracy of ML-$\omega$PBE because the critical MOs are not very delocalized. If we revisit Figures S3 through S7, we realize that frontier MOs of radicals occupy similar space to their hydrogenated counterparts or are slightly more localized.

Also, the inclusion of TDA slightly compromises the accuracy of $E_{\text{abs}}$ and $E_{\text{fl}}$, indicating that these radicals are less likely to suffer from the instability problems like some organic semiconducting molecules and it is necessary to include de-excitation and coupling matrices in the working eigenvalue equations of linear response.[49,55–59]

## 4 Conclusion

In the prsent study, we perform a follow-up assessment study for ML-$\omega$PBE,[80] which was self-developed based on the top-down SEML strategy,[88–93] and expand its application domain from closed-shell organic semiconducting molecules[100–105] to doublet-spin organic semiconducting radicals[17,113–158] in the framework of single-reference DFT and TDDFT. Even with only closed-shell molecules in the training set, ML-$\omega$PBE reproduces the molecule-dependent values of $\omega$ generated by OT-$\omega$PBE with a MAE of 0.0197 $a_0^{-1}$ over all doublet-spin radicals in the test set, but reduces the average computational cost by 2.46 orders of magnitude.

Due to accurate captures of electronic structures, ML-$\omega$PBE demonstrates an analogous

top predictive power to OT-$\omega$PBE regarding experimentally observable $E_{\text{abs}}$ and $E_{\text{fl}}$ for most radicals, and outperforms every other XC functionals in discussion[50–52,70,75,81,106–109] without prominent error cancellations. The only exception is the aryl oxygen-based family for which all single-reference DFT methods fail to obtain correct energy orders of frontier MOs.

In summary, through our study we validate and strengthen the practical value of ML-$\omega$PBE in deciphering and predicting optical properties for luminescent organic semiconducting radicals and facilitate its application in large-scale computationally aided materials discovery for various emergent areas.

## Acknowledgement

The authors would like to acknowledge the UMass/URI Unity Cluster and MIT SuperCloud[194] for providing high-performance computing (HPC) resources. Z.L. would like to acknowledge UMass Amherst for providing the start-up funds to accomplish this study. Also, we would like to thank the helpful discussions with Prof. Hui Guan, Dr. Kun Yao, Dr. Lixue (Sherry) Cheng, Dr. Xin Chen, and Mr. Junjie Yang.

## Supporting Information Available

The Supporting Information is available free of charge at XXXXXXXXX.

- Brief revisit of the SEML model; error statistics of ML-$\omega$PBE and other XC functionals in optical properties; and configurations of frontier MOs and NTOs (PDF).
- Optimized $D_0$ geometries for 48 radicals in the test subset of $E_{\text{abs}}$; and optimized $D_1$ geometries for 16 radicals in the test subset of $E_{\text{fl}}$ (ZIP).
- SMILES strings, experimental measurements of $E_{\text{abs}}$ and $E_{\text{fl}}$, values of $\omega_{\text{OT}}$ and $\omega_{\text{ML}}$ for all 64 radicals in the external test set (XLSX).

# References


(1) Gryn'ova, G.; Marshall, D. L.; Blanksby, S. J.; Coote, M. L. Switching Radical Stability by pH-Induced Orbital Conversion. *Nat. Chem.* **2013**, *5*, 474–481.

(2) Kumar, A.; Sevilla, M. D. SOMO–HOMO Level Inversion in Biologically Important Radicals. *J. Phys. Chem. B* **2018**, *122*, 98–105.

(3) Reineke, S. Radically More Stable. *Nat. Mater.* **2019**, *18*, 917–918.

(4) Guo, H.; Peng, Q.; Chen, X.-K.; Gu, Q.; Dong, S.; Evans, E. W.; Gillett, A. J.; Ai, X.; Zhang, M.; Credgington, D. et al. High Stability and Luminescence Efficiency in Donor–Acceptor Neutral Radicals not Following the Aufbau Principle. *Nat. Mater.* **2019**, *18*, 977–984.

(5) Tanushi, A.; Kimura, S.; Kusamoto, T.; Tominaga, M.; Kitagawa, Y.; Nakano, M.; Nishihara, H. NIR Emission and Acid-Induced Intramolecular Electron Transfer Derived from a SOMO–HOMO Converted Non-Aufbau Electronic Structure. *J. Phys. Chem. C* **2019**, *123*, 4417–4423.

(6) Cho, E.; Coropceanu, V.; Brédas, J.-L. Organic Neutral Radical Emitters: Impact of Chemical Substitution and Electronic-State Hybridization on the Luminescence Properties. *J. Am. Chem. Soc.* **2020**, *142*, 17782–17786.

(7) Abdurahman, A.; Hele, T. J. H.; Gu, Q.; Zhang, J.; Peng, Q.; Zhang, M.; Friend, R. H.; Li, F.; Evans, E. W. Understanding the Luminescent Nature of Organic Radicals for Efficient Doublet Emitters and Pure-Red Light-Emitting Diodes. *Nat. Mater.* **2020**, *19*, 1224–1229.

(8) Abella, L.; Crassous, J.; Favereau, L.; Autschbach, J. Why is the Energy of the Singly Occupied Orbital in Some Radicals below the Highest Occupied Orbital Energy? *Chem. Mater.* **2021**, *33*, 3678–3691.

(9) Kasemthaveechok, S.; Abella, L.; Crassous, J.; Autschbach, J.; Favereau, L. Organic Radicals With Inversion of SOMO and HOMO Energies and Potential Applications in Optoelectronics. *Chem. Sci.* **2022**, *13*, 9833–9847.

(10) Miller, J. S. Organic- and Molecule-Based Magnets. *Mater. Today* **2014**, *17*, 224–235.

(11) Jiao, Y.; Liu, K.; Wang, G.; Wang, Y.; Zhang, X. Supramolecular Free Radicals: Near-Infrared Organic Materials with Enhanced Photothermal Conversion. *Chem. Sci.* **2015**, *6*, 3975–3980.

(12) Jung, H. S.; Verwilst, P.; Sharma, A.; Shin, J.; Sessler, J. L.; Kim, J. S. Organic Molecule-Based Photothermal Agents: An Expanding Photothermal Therapy Universe. *Chem. Soc. Rev.* **2018**, *47*, 2280–2297.

(13) Yang, Y.; He, P.; Wang, Y.; Bai, H.; Wang, S.; Xu, J.-F.; Zhang, X. Supramolecular Radical Anions Triggered by Bacteria *In-Situ* for Selective Photothermal Therapy. *Angew. Chem. Int. Ed.* **2017**, *56*, 16239–16242.

(14) Xia, R.; Zheng, X.; Hu, X.; Liu, S.; Xie, Z. Photothermal-Controlled Generation of Alkyl Radical from Organic Nanoparticles for Tumor Treatment. *ACS Appl. Mater. Interfaces* **2019**, *11*, 5782–5790.

(15) Tang, B.; Li, W.-L.; Chang, Y.; Yuan, B.; Wu, Y.; Zhang, M.-T.; Xu, J.-F.; Li, J.; Zhang, X. A Supramolecular Radical Dimer: High-Efficiency NIR-II Photothermal Conversion and Therapy. *Angew. Chem. Int. Ed.* **2019**, *58*, 15526–15531.

(16) Peng, Q.; Obolda, A.; Zhang, M.; Li, F. Organic Light-Emitting Diodes Using a Neutral $\pi$-Radical as Emitter: The Emission from a Doublet. *Angew. Chem. Int. Ed.* **2015**, *54*, 7091–7095.

(17) Ai, X.; Evans, E. W.; Dong, S.; Gillett, A. J.; Guo, H.; Chen, Y.; Hele, T. J.;

Friend, R. H.; Li, F. Efficient Radical-Based Light-Emitting Diodes with Doublet Emission. *Nature* **2018**, *563*, 536–540.

(18) Hudson, J. M.; Hele, T. J. H.; Evans, E. W. Efficient Light-Emitting Diodes from Organic Radicals with Doublet Emission. *J. Appl. Phys.* **2021**, *129*, 180901.

(19) Slater, J. C. The Theory of Complex Spectra. *Phys. Rev.* **1929**, *34*, 1293–1322.

(20) Li Manni, G.; Carlson, R. K.; Luo, S.; Ma, D.; Olsen, J.; Truhlar, D. G.; Gagliardi, L. Multiconfiguration Pair-Density Functional Theory. *J. Chem. Theory Comput.* **2014**, *10*, 3669–3680.

(21) Gagliardi, L.; Truhlar, D. G.; Li Manni, G.; Carlson, R. K.; Hoyer, C. E.; Bao, J. L. Multiconfiguration Pair-Density Functional Theory: A New Way To Treat Strongly Correlated Systems. *Acc. Chem. Res.* **2017**, *50*, 66–73.

(22) Baer, R.; Livshits, E.; Salzner, U. Tuned Range-Separated Hybrids in Density Functional Theory. *Annu. Rev. Phys. Chem.* **2010**, *61*, 85–109.

(23) Li, Z.; Liu, W. Critical Assessment of TD-DFT for Excited States of Open-Shell Systems: I. Doublet–Doublet Transitions. *J. Chem. Theory Comput.* **2016**, *12*, 238–260.

(24) Li, Z.; Liu, W. Critical Assessment of Time-Dependent Density Functional Theory for Excited States of Open-Shell Systems: II. Doublet-Quartet Transitions. *J. Chem. Theory Comput.* **2016**, *12*, 2517–2527.

(25) Suo, B.; Shen, K.; Li, Z.; Liu, W. Performance of TD-DFT for Excited States of Open-Shell Transition Metal Compounds. *J. Phys. Chem. A* **2017**, *121*, 3929–3942.

(26) Wang, Z.; Li, Z.; Zhang, Y.; Liu, W. Analytic Energy Gradients of Spin-Adapted Open-Shell Time-Dependent Density Functional Theory. *J. Chem. Phys.* **2020**, *153*, 164109.

(27) Shao, Y.; Head-Gordon, M.; Krylov, A. I. The Spin–Flip Approach within Time-Dependent Density Functional Theory: Theory and Applications to Diradicals. *J. Chem. Phys.* **2003**, *118*, 4807–4818.

(28) Bernard, Y. A.; Shao, Y.; Krylov, A. I. General Formulation of Spin-Flip Time-Dependent Density Functional Theory Using Non-Collinear Kernels: Theory, Implementation, and Benchmarks. *J. Chem. Phys.* **2012**, *136*, 204103.

(29) Hait, D.; Head-Gordon, M. Highly Accurate Prediction of Core Spectra of Molecules at Density Functional Theory Cost: Attaining Sub-Electronvolt Error from a Restricted Open-Shell Kohn–Sham Approach. *J. Phys. Chem. Lett.* **2020**, *11*, 775–786.

(30) Hait, D.; Head-Gordon, M. Excited State Orbital Optimization via Minimizing the Square of the Gradient: General Approach and Application to Singly and Doubly Excited States via Density Functional Theory. *J. Chem. Theory Comput.* **2020**, *16*, 1699–1710.

(31) Hait, D.; Head-Gordon, M. Orbital Optimized Density Functional Theory for Electronic Excited States. *J. Phys. Chem. Lett.* **2021**, *12*, 4517–4529.

(32) Hait, D.; Haugen, E. A.; Yang, Z.; Oosterbaan, K. J.; Leone, S. R.; Head-Gordon, M. Accurate Prediction of Core-Level Spectra of Radicals at Density Functional Theory Cost via Square Gradient Minimization and Recoupling of Mixed Configurations. *J. Chem. Phys.* **2020**, *153*, 134108.

(33) Limacher, P. A.; Ayers, P. W.; Johnson, P. A.; De Baerdemacker, S.; Van Neck, D.; Bultinck, P. A New Mean-Field Method Suitable for Strongly Correlated Electrons: Computationally Facile Antisymmetric Products of Nonorthogonal Geminals. *J. Chem. Theory Comput.* **2013**, *9*, 1394–1401.

(34) Sun, Q.; Yang, J.; Chan, G. K.-L. A General Second Order Complete Active Space

Self-Consistent-Field Solver for Large-Scale Systems. *Chem. Phys. Lett.* **2017**, *683*, 291–299.

(35) Mostafanejad, M.; DePrince, A. E. Combining Pair-Density Functional Theory and Variational Two-Electron Reduced-Density Matrix Methods. *J. Chem. Theory Comput.* **2019**, *15*, 290–302.

(36) Hirata, S.; Lee, T. J.; Head-Gordon, M. Time-Dependent Density Functional Study on the Electronic Excitation Energies of Polycyclic Aromatic Hydrocarbon Radical Cations of Naphthalene, Anthracene, Pyrene, and Perylene. *J. Chem. Phys.* **1999**, *111*, 8904–8912.

(37) Tokmachev, A. M.; Boggio-Pasqua, M.; Mendive-Tapia, D.; Bearpark, M. J.; Robb, M. A. Fluorescence of the Perylene Radical Cation and an Inaccessible $D_0/D_1$ Conical Intersection: An MMVB, RASSCF, and TD-DFT Computational Study. *J. Chem. Phys.* **2010**, *132*, 044306.

(38) Weisman, J. L.; Lee, T. J.; Salama, F.; Head-Gordon, M. Time-dependent Density Functional Theory Calculations of Large Compact Polycyclic Aromatic Hydrocarbon Cations: Implications for the Diffuse Interstellar Bands. *Astrophys. J.* **2003**, *587*, 256–261.

(39) Malloci, G.; Mulas, G.; Cappellini, G.; Joblin, C. Time-Dependent Density Functional Study of the Electronic Spectra of Oligoacenes in the Charge States $-1$, 0, $+1$, and $+2$. *Chem. Phys.* **2007**, *340*, 43–58.

(40) Bauschlicher, C. W. Time-Dependent Density Functional Theory for Polycyclic Aromatic Hydrocarbon Anions: What is the Best Approach. *Chem. Phys. Lett.* **2005**, *409*, 235–239.

(41) Riffet, V.; Jacquemin, D.; Cauët, E.; Frison, G. Benchmarking DFT and TD-DFT

Functionals for the Ground and Excited States of Hydrogen-Rich Peptide Radicals. *J. Chem. Theory Comput.* **2014**, *10*, 3308–3318.

(42) Tureček, F. Benchmarking Electronic Excitation Energies and Transitions in Peptide Radicals. *J. Phys, Chem. A* **2015**, *119*, 10101–10111.

(43) Boggio-Pasqua, M.; Bearpark, M. J. Using Density Functional Theory Based Methods to Investigate the Photophysics of Polycyclic Aromatic Hydrocarbon Radical Cations: A Benchmark Study on Naphthalene, Pyrene and Perylene Cations. *ChemPhotoChem* **2019**, *3*, 763–769.

(44) Weisman, J. L.; Lee, T. J.; Head-Gordon, M. Electronic Spectra and Ionization Potentials of a Stable Class of Closed Shell Polycyclic Aromatic Hydrocarbon Cations. *Spectrochim. Acta A* **2001**, *57*, 931–945.

(45) Hirata, S.; Head-Gordon, M.; Szczepanski, J.; Vala, M. Time-Dependent Density Functional Study of the Electronic Excited States of Polycyclic Aromatic Hydrocarbon Radical Ions. *J. Phys. Chem. A* **2003**, *107*, 4940–4951.

(46) Chai, J.-D.; Head-Gordon, M. Systematic Optimization of Long-Range Corrected Hybrid Density Functionals. *J. Chem. Phys.* **2008**, *128*, 084106.

(47) Bera, P. P.; Head-Gordon, M.; Lee, T. J. Initiating Molecular Growth in the Interstellar Medium via Dimeric Complexes of Observed Ions and Molecules. *Astron. Astrophys.* **2011**, *535*, A74.

(48) Bera, P. P.; Head-Gordon, M.; Lee, T. J. Relative Energies, Structures, Vibrational Frequencies, and Electronic Spectra of Pyrylium Cation, an Oxygen-Containing Carbocyclic Ring Isoelectronic with Benzene, and its Isomers. *J. Chem. Phys.* **2013**, *139*, 174302.

(49) Hirata, S.; Head-Gordon, M. Time-Dependent Density Functional Theory within the Tamm–Dancoff Approximation. *Chem. Phys. Lett.* **1999**, *314*, 291–299.

(50) Becke, A. D. Density-Functional Exchange-Energy Approximation with Correct Asymptotic Behavior. *Phys. Rev. A* **1988**, *38*, 3098–3100.

(51) Lee, C.; Yang, W.; Parr, R. G. Development of the Colle–Salvetti Correlation-Energy Formula into a Functional of the Electron Density. *Phys. Rev. B* **1988**, *37*, 785–789.

(52) Becke, A. D. A New Mixing of Hartree–Fock and Local Density-Functional Theories. *J. Chem. Phys.* **1993**, *98*, 1372–1377.

(53) Dreuw, A.; Head-Gordon, M. Failure of Time-Dependent Density Functional Theory for Long-Range Charge-Transfer Excited States: the Zincbacteriochlorin–Bacteriochlorin and Bacteriochlorophyll–Spheroidene Complexes. *J. Am. Chem. Soc.* **2004**, *126*, 4007–4016.

(54) Dreuw, A.; Head-Gordon, M. Single-Eeference *Ab Initio* Methods for the Calculation of Excited States of Large Molecules. *Chem. Rev.* **2005**, *105*, 4009–4037.

(55) Wang, Y.-L.; Wu, G.-S. Improving the TDDFT Calculation of Low-Lying Excited States for Polycyclic Aromatic Hydrocarbons Using the Tamm–Dancoff Approximation. *Int. J Quantum Chem.* **2008**, *108*, 430–439.

(56) Hsu, C.-P.; Hirata, S.; Head-Gordon, M. Excitation Energies from Time-Dependent Density Functional Theory for Linear Polyene Oligomers: Butadiene to Decapentaene. *J. Phys. Chem. A* **2001**, *105*, 451–458.

(57) Bauernschmitt, R.; Ahlrichs, R. Stability Analysis for Solutions of the Closed Shell Kohn–Sham Equation. *J. Chem. Phys.* **1996**, *104*, 9047–9052.

(58) Sears, J. S.; Körzdörfer, T.; Zhang, C.-R.; Brédas, J.-L. Communication: Orbital

Instabilities and Triplet States from Time-Dependent Density Functional Theory and Long-Range Corrected Functionals. *J. Chem. Phys.* **2011**, *135*, 151103.

(59) Yamada, T.; Hirata, S. Singlet and Triplet Instability Theorems. *J. Chem. Phys.* **2015**, *143*, 114112.

(60) Malloci, G.; Joblin, C.; Mulas, G. On-Line Database of the Spectral Properties of Polycyclic Aromatic Hydrocarbons. *Chem. Phys.* **2007**, *332*, 353–359.

(61) Malloci, G.; Mulas, G.; Joblin, C. Electronic Absorption Spectra of PAHs Up to Vacuum UV – Towards a Detailed Model of Interstellar PAH Photophysics. *Astron. Astrophys.* **2004**, *426*, 105–117.

(62) Rapacioli, M.; Simon, A.; Marshall, C. C. M.; Cuny, J.; Kokkin, D.; Spiegelman, F.; Joblin, C. Cationic Methylene–Pyrene Isomers and Isomerization Pathways: Finite Temperature Theoretical Studies. *J. Phys. Chem. A* **2015**, *119*, 12845–12854.

(63) Dierksen, M.; Grimme, S. Density Functional Calculations of the Vibronic Structure of Electronic Absorption Spectra. *J. Chem. Phys.* **2004**, *120*, 3544–3554.

(64) Dierksen, M.; Grimme, S. The Vibronic Structure of Electronic Absorption Spectra of Large Molecules: A Time-Dependent Density Functional Study on the Influence of "Exact" Hartree–Fock Exchange. *J. Phys. Chem. A* **2004**, *108*, 10225–10237.

(65) Send, R.; Kühn, M.; Furche, F. Assessing Excited State Methods by Adiabatic Excitation Energies. *J. Chem. Theory Comput.* **2011**, *7*, 2376–2386.

(66) Bates, J. E.; Furche, F. Harnessing the Meta-Generalized Gradient Approximation for Time-Dependent Density Functional Theory. *J. Chem. Phys.* **2012**, *137*, 164105.

(67) Bates, J. E.; Heiche, M. C.; Liang, J.; Furche, F. Erratum: "Harnessing the Meta-Generalized Gradient Approximation for Time-Dependent Density Functional Theory" [J. Chem. Phys. 137, 164105 (2012)]. *J. Chem. Phys.* **2022**, *156*, 159902.

(68) Barnes, L.; Abdul-Al, S.; Allouche, A.-R. TDDFT Assessment of Functionals for Optical 0–0 Transitions in Small Radicals. *J. Phys. Chem. A* **2014**, *118*, 11033–11046.

(69) Chai, J.-D.; Head-Gordon, M. Long-Range Corrected Hybrid Density Functionals with Damped Atom–Atom Dispersion Corrections. *Phys. Chem. Chem. Phys.* **2008**, *10*, 6615–6620.

(70) Lin, Y.-S.; Li, G.-D.; Mao, S.-P.; Chai, J.-D. Long-Range Corrected Hybrid Density Functionals with Improved Dispersion Corrections. *J. Chem. Theory Comput.* **2013**, *9*, 263–272.

(71) Mardirossian, N.; Head-Gordon, M. $\omega$B97X-V: A 10-Parameter, Range-Separated Hybrid, Generalized Gradient Approximation Density Functional with Nonlocal Correlation, Designed by a Survival-of-the-Fittest Strategy. *Phys. Chem. Chem. Phys.* **2014**, *16*, 9904–9924.

(72) Henderson, T. M.; Janesko, B. G.; Scuseria, G. E. Generalized Gradient Approximation Model Exchange Holes for Range-Separated Hybrids. *J. Chem. Phys.* **2008**, *128*, 194105.

(73) Heyd, J.; Scuseria, G. E.; Ernzerhof, M. Hybrid Functionals Based on a Screened Coulomb Potential. *J. Chem. Phys.* **2003**, *118*, 8207–8215.

(74) Krukau, A. V.; Vydrov, O. A.; Izmaylov, A. F.; Scuseria, G. E. Influence of the Exchange Screening Parameter on the Performance of Screened Hybrid Functionals. *J. Chem. Phys.* **2006**, *125*, 224106.

(75) Rohrdanz, M. A.; Herbert, J. M. Simultaneous Benchmarking of Ground- and Excited-State Properties with Long-Range-Corrected Density Functional Theory. *J. Chem. Phys.* **2008**, *129*, 034107.

(76) Rohrdanz, M. A.; Martins, K. M.; Herbert, J. M. A Long-Range-Corrected Density Functional that Performs Well for Both Ground-State Properties and Time-Dependent Density Functional Theory Excitation Energies, Including Charge-Transfer Excited States. *J. Chem. Phys.* **2009**, *130*, 054112.

(77) Mardirossian, N.; Head-Gordon, M. $\omega$B97M-V: A Combinatorially Optimized, Range-Separated Hybrid, *meta*-GGA Density Functional with VV10 Nonlocal Correlation. *J. Chem. Phys.* **2016**, *144*, 214110.

(78) Zhang, Y.; Xu, X.; Goddard, W. A. Doubly Hybrid Density Functional for Accurate Descriptions of Nonbond Interactions, Thermochemistry, and Thermochemical Kinetics. *Proc. Natl. Acad. Sci.* **2009**, *106*, 4963–4968.

(79) Lin, Z.; Van Voorhis, T. Triplet Tuning: A Novel Family of Non-Empirical Exchange–Correlation Functionals. *J. Chem. Theory Comput.* **2019**, *15*, 1226–1241.

(80) Ju, C.-W.; French, E. J.; Geva, N.; Kohn, A. W.; Lin, Z. Stacked Ensemble Machine Learning for Range-Separation Parameters. *J. Phys. Chem. Lett.* **2021**, *12*, 9516–9524.

(81) Perdew, J. P.; Burke, K.; Ernzerhof, M. Generalized Gradient Approximation Made Simple. *Phys. Rev. Lett.* **1996**, *77*, 3865.

(82) Kronik, L.; Stein, T.; Refaely-Abramson, S.; Baer, R. Excitation Gaps of Finite-Sized Systems from Optimally Tuned Range-Separated Hybrid Functionals. *J. Chem. Theory Comput.* **2012**, *8*, 1515–1531.

(83) Livshits, E.; Baer, R. A Well-Tempered Density Functional Theory of Electrons in Molecules. *Phys. Chem. Chem. Phys.* **2007**, *9*, 2932–2941.

(84) Stein, T.; Kronik, L.; Baer, R. Reliable Prediction of Charge Transfer Excitations in Molecular Complexes Using Time-Dependent Density Functional Theory. *J. Am. Chem. Soc.* **2009**, *131*, 2818–2820.

(85) Stein, T.; Eisenberg, H.; Kronik, L.; Baer, R. Fundamental Gaps in Finite Systems from Eigenvalues of a Generalized Kohn–Sham Method. *Phys. Rev. Lett.* **2010**, *105*, 266802.

(86) Kuritz, N.; Stein, T.; Baer, R.; Kronik, L. Charge-Transfer-Like $\pi \rightarrow \pi^*$ Excitations in Time-Dependent Density Functional Theory: A Conundrum and Its Solution. *J. Chem. Theory Comput.* **2011**, *7*, 2408–2415.

(87) Koopmans, T. Über die Zuordnung von Wellenfunktionen und Eigenwerten zu den Einzelnen Elektronen Eines Atoms. *Physica* **1934**, *1*, 104–113.

(88) Wolpert, D. H. Stacked Generalization. *Neural Netw.* **1992**, *5*, 241–259.

(89) Polikar, R. Ensemble Based Systems in Decision Making. *IEEE Circuits Syst. Mag.* **2006**, *6*, 21–45.

(90) Rokach, L. Ensemble-Based Classifiers. *Artif. Intell. Rev.* **2010**, *33*, 1–39.

(91) Opitz, D.; Maclin, R. Popular Ensemble Methods: An Empirical Study. *J. Artif. Intell. Res.* **1999**, *11*, 169–198.

(92) Coscrato, V.; de Almeida Inácio, M. H.; Izbicki, R. The NN-Stacking: Feature Weighted Linear Stacking through Neural Networks. *Neurocomputing* **2020**, *399*, 141–152.

(93) Breiman, L. Stacked Regressions. *Mach. Learn.* **1996**, *24*, 49–64.

(94) Yang, Q.; Li, Y.; Yang, J.-D.; Liu, Y.; Zhang, L.; Luo, S.; Cheng, J.-P. Holistic Prediction of the p$K_a$ in Diverse Solvents Based on a Machine-Learning Approach. *Angew. Chem. Int. Ed.* **2020**, *59*, 19282–19291.

(95) Rogers, D.; Hahn, M. Extended-Connectivity Fingerprints. *J. Chem. Inf. Model.* **2010**, *50*, 742–754.

(96) Willighagen, E. L.; Mayfield, J. W.; Alvarsson, J.; Berg, A.; Carlsson, L.; Jeliazkova, N.; Kuhn, S.; Pluskal, T.; Rojas-Chertó, M.; Spjuth, O. et al. The Chemistry Development Kit (CDK) v2.0: Atom Typing, Depiction, Molecular Formulas, and Substructure Searching. *J. Cheminf.* **2017**, *9*, 1–19.

(97) Grimme, S.; Bannwarth, C.; Shushkov, P. A Robust and Accurate Tight-Binding Quantum Chemical Method for Structures, Vibrational Frequencies, and Noncovalent Interactions of Large Molecular Systems Parametrized for All *spd*-Block Elements ($Z = 1 - 86$). *J. Chem. Theory Comput.* **2017**, *13*, 1989–2009.

(98) Bannwarth, C.; Ehlert, S.; Grimme, S. GFN2-xTB–An Accurate and Broadly Parametrized Self-Consistent Tight-Binding Quantum Chemical Method with Multipole Electrostatics and Density-Dependent Dispersion Contributions. *J. Chem. Theory Comput.* **2019**, *15*, 1652–1671.

(99) Pracht, P.; Caldeweyher, E.; Ehlert, S.; Grimme, S. A Robust Non-Self-Consistent Tight-Binding Quantum Chemistry Method for Large Molecules. *ChemRxiv* **2019**, doi: 10.26434/chemrxiv.8326202.v1.

(100) Hachmann, J.; Olivares-Amaya, R.; Atahan-Evrenk, S.; Amador-Bedolla, C.; Sánchez-Carrera, R. S.; Gold-Parker, A.; Vogt, L.; Brockway, A. M.; Aspuru-Guzik, A. The Harvard Clean Energy Project: Large-Scale Computational Screening and Design of Organic Photovoltaics on the World Community Grid. *J. Phys. Chem. Lett.* **2011**, *2*, 2241–2251.

(101) Hachmann, J.; Olivares-Amaya, R.; Jinich, A.; Appleton, A. L.; Blood-Forsythe, M. A.; Seress, L. R.; Román-Salgado, C.; Trepte, K.; Atahan-Evrenk, S.; Er, S. et al. Lead Candidates for High-Performance Organic Photovoltaics from High-Throughput Quantum Chemistry–the Harvard Clean Energy Project. *Energy Environ. Sci.* **2014**, *7*, 698–704.

(102) Ramsundar, B.; Eastman, P.; Walters, P.; Pande, V. *Deep Learning for the Life Sciences: Applying Deep Learning to Genomics, Microscopy, Drug Discovery, and More*; O'Reilly Media, 2019.

(103) Ju, C.-W.; Bai, H.; Li, B.; Liu, R. Machine Learning Enables Highly Accurate Predictions of PhotoPhysical Properties of Organic Fluorescent Materials: Emission Wavelengths and Quantum Yields. *J. Chem. Inf. Model.* **2021**, *61*, 1053–1065.

(104) Lopez, S. A.; Pyzer-Knapp, E. O.; Simm, G. N.; Lutzow, T.; Li, K.; Seress, L. R.; Hachmann, J.; Aspuru-Guzik, A. The Harvard Organic Photovoltaic Dataset. *Sci. Data* **2016**, *3*, 160086.

(105) Gómez-Bombarelli, R.; Aguilera-Iparraguirre, J.; Hirzel, T. D.; Duvenaud, D.; Maclaurin, D.; Blood-Forsythe, M. A.; Chae, H. S.; Einzinger, M.; Ha, D.-G.; Wu, T. et al. Design of Efficient Molecular Organic Light-Emitting Diodes by a High-Throughput Virtual Screening and Experimental Approach. *Nat. Mater.* **2016**, *15*, 1120–1127.

(106) Perdew, J. P.; Ernzerhof, M.; Burke, K. Rationale for Mixing Exact Exchange with Density Functional Approximations. *J. Chem. Phys.* **1996**, *105*, 9982–9985.

(107) Adamo, C.; Barone, V. Toward Reliable Density Functional Methods without Adjustable Parameters: The PBE0 Model. *J. Chem. Phys.* **1999**, *110*, 6158–6170.

(108) Yanai, T.; Tew, D. P.; Handy, N. C. A New Hybrid Exchange–Correlation Functional Using the Coulomb-Attenuating Method (CAM-B3LYP). *Chem. Phys. Lett.* **2004**, *393*, 51–57.

(109) Zhao, Y.; Truhlar, D. G. The M06 Suite of Density Functionals for Main Group Thermochemistry, Thermochemical Kinetics, Noncovalent Interactions, Excited States, and Transition Elements: Two New Functionals and Systematic Testing of Four M06-Class Functionals and 12 Other Functionals. *Theor. Chem. Acc.* **2008**, *120*, 215–241.

(110) Gong, J.; Lam, J. W. Y.; Tang, B. Z. Benchmark and Parameter Tuning of Hybrid Functionals for Fast Calculation of Excitation Energies of AIEgens. *Phys. Chem. Chem. Phys.* **2020**, *22*, 18035–18039.

(111) Ali, A.; Rafiq, M. I.; Zhang, Z.; Cao, J.; Geng, R.; Zhou, B.; Tang, W. TD-DFT Benchmark for UV-Visible Spectra of Fused-Ring Electron Acceptors Using Global and Range-Separated Hybrids. *Phys. Chem. Chem. Phys.* **2020**, *22*, 7864–7874.

(112) Alipour, M.; Safari, Z. Photophysics of OLED Materials with Emitters Exhibiting Thermally Activated Delayed Fluorescence and Used in Hole/Electron Transporting Layer from Optimally Tuned Range-Separated Density Functional Theory. *J. Phys. Chem. C* **2018**, *123*, 746–761.

(113) Bejarano, F.; Olavarria-Contreras, I. J.; Droghetti, A.; Rungger, I.; Rudnev, A.; Gutiérrez, D.; Mas-Torrent, M.; Veciana, J.; van der Zant, H. S. J.; Rovira, C. et al. Robust Organic Radical Molecular Junctions Using Acetylene Terminated Groups for C−Au Bond Formation. *J. Am. Chem. Soc.* **2018**, *140*, 1691–1696.

(114) Hattori, Y.; Kusamoto, T.; Sato, T.; Nishihara, H. Synergistic Luminescence Enhancement of a Pyridyl-Substituted Triarylmethyl Radical Based on Fluorine Substitution and Coordination to Gold. *Chem. Commun.* **2016**, *52*, 13393–13396.

(115) Ai, X.; Chen, Y.; Feng, Y.; Li, F. A Stable Room-Temperature Luminescent Biphenylmethyl Radical. *Angew. Chem. Int. Ed.* **2018**, *57*, 2869–2873.

(116) Dong, S.; Xu, W.; Guo, H.; Yan, W.; Zhang, M.; Li, F. Effects of Substituents on Luminescent Efficiency of Stable Triaryl Methyl Radicals. *Phys. Chem. Chem. Phys.* **2018**, *20*, 18657–18662.

(117) Abdurahman, A.; Chen, Y.; Ai, X.; Ablikim, O.; Gao, Y.; Dong, S.; Li, B.; Yang, B.; Zhang, M.; Li, F. A Pure Red Luminescent $\beta$-Carboline-Substituted Biphenylmethyl

Radical: Photophysics, Stability and OLEDs. *J. Mater. Chem. C* **2018**, *6*, 11248–11254.

(118) Rösel, S.; Becker, J.; Allen, W. D.; Schreiner, P. R. Probing the Delicate Balance between Pauli Repulsion and London Dispersion with Triphenylmethyl Derivatives. *J. Am. Chem. Soc.* **2018**, *140*, 14421–14432.

(119) Fischer, H.; Baer, R.; Hany, R.; Verhoolen, I.; Walbiner, M. 2,2-Dimethoxy-2-Phenylacetophenone: Photochemistry and Free Radical Photofragmentation. *J. Chem. Soc., Perkin Trans. 2* **1990**, 787–798.

(120) López, M.; Velasco, D.; López-Calahorra, F.; Juliá, L. Light-Emitting Persistent Radicals for Efficient Sensor Devices of Solvent Polarity. *Tetrahedron Lett.* **2008**, *49*, 5196–5199.

(121) Gao, Y.; Xu, W.; Ma, H.; Obolda, A.; Yan, W.; Dong, S.; Zhang, M.; Li, F. Novel Luminescent Benzimidazole-Substituent Tris(2,4,6-Trichlorophenyl)Methyl Radicals: Photophysics, Stability, and Highly Efficient Red-Orange Electroluminescence. *Chem. Mater.* **2017**, *29*, 6733–6739.

(122) Wu, X.; Kim, J. O.; Medina, S.; Ramírez, F. J.; Mayorga Burrezo, P.; Wu, S.; Lim, Z. L.; Lambert, C.; Casado, J.; Kim, D. et al. Push–Pull-Type Polychlorotriphenylmethyl Radicals: New Two-Photon Absorbers and Dyes for Generation of Photo-Charges. *Chem. Eur. J.* **2017**, *23*, 7698–7702.

(123) Gu, X.; Gopalakrishna, T. Y.; Phan, H.; Ni, Y.; Herng, T. S.; Ding, J.; Wu, J. A Three-Dimensionally $\pi$-Conjugated Diradical Molecular Cage. *Angew. Chem. Int. Ed.* **2017**, *56*, 15383–15387.

(124) Heckmann, A.; Lambert, C.; Goebel, M.; Wortmann, R. Synthesis and Photophysics of a Neutral Organic Mixed-Valence Compound. *Angew. Chem. Int. Ed.* **2004**, *43*, 5851–5856.

(125) Ballester, M.; Riera, J.; Castaner, J.; Rodriguez, A.; Rovira, C.; Veciana, J. Inert Carbon Free Radicals. 3. Monofunctionalized Radicals From Perchlorotriphenylcarbenium Hexachloroantimonate. *J. Org. Chem.* **1982**, *47*, 4498–4505.

(126) Bonvoisin, J.; Launay, J.-P.; Rovira, C.; Veciana, J. Purely Organic Mixed-Valence Molecules with Nanometric Dimensions Showing Long-Range Electron Transfer. Synthesis, and Optical and EPR Studies of a Radical Anion Derived from a Bis(Triarylmethyl)Diradical. *Angew. Chem. Int. Ed.* **1994**, *33*, 2106–2109.

(127) Teruel, L.; Viadel, L.; Carilla, J.; Fajarí, L.; Brillas, E.; Sañé, J.; Rius, J.; Juliá, L. (4-Amino-2, 6-Dichlorophenyl)-bis (2, 4, 6-Trichlorophenyl) Methyl Radical: A New Constituent of Organic Magnetic Materials. *J. Org. Chem.* **1996**, *61*, 6063–6066.

(128) Neckers, D.; Rajadurai, S.; Valdes-Aguilera, O.; Zakrzewski, A.; Linden, S. Photophysics and Photochemistry of P-Benzoylphenyldiphenylmethyl in Solution. *Tetrahedron Lett.* **1988**, *29*, 5109–5112.

(129) Ruberu, S. R.; Fox, M. A. Photochemical Behavior of Stable Free Radicals: The Photochemistry of Perchlorodiphenylmethyl Radical. *J. Phys. Chem.* **1993**, *97*, 143–149.

(130) Peng, Q.; Obolda, A.; Zhang, M.; Li, F. Organic Light-Emitting Diodes Using a Neutral $\pi$ Radical as Emitter: The Emission from a Doublet. *Angew. Chem. Int. Ed.* **2015**, *54*, 7091–7095.

(131) Cui, Z.; Ye, S.; Wang, L.; Guo, H.; Obolda, A.; Dong, S.; Chen, Y.; Ai, X.; Abdurahman, A.; Zhang, M. et al. Radical-Based Organic Light-Emitting Diodes with Maximum External Quantum Efficiency of 10.6%. *J. Phys. Chem. Lett.* **2018**, *9*, 6644–6648.

(132) Jin, Q.; Chen, S.; Sang, Y.; Guo, H.; Dong, S.; Han, J.; Chen, W.; Yang, X.; Li, F.;

Duan, P. Circularly Polarized Luminescence of Achiral Open-Shell $\pi$-Radicals. *Chem. Commun.* **2019**, *55*, 6583–6586.

(133) Hattori, Y.; Kusamoto, T.; Nishihara, H. Highly Photostable Luminescent Open-Shell (3,5-Dihalo-4-Pyridyl)bis(2,4,6-Trichlorophenyl)Methyl Radicals: Significant Effects of Halogen Atoms on Their Photophysical and Photochemical Properties. *RSC Adv.* **2015**, *5*, 64802–64805.

(134) Uchida, K.; Mou, Z.; Kertesz, M.; Kubo, T. Fluxional $\sigma$-Bonds of the 2,5,8-Trimethylphenalenyl Dimer: Direct Observation of the Sixfold $\sigma$-Bond Shift via a $\pi$-Dimer. *J. Am. Chem. Soc.* **2016**, *138*, 4665–4672.

(135) Small, D.; Zaitsev, V.; Jung, Y.; Rosokha, S. V.; Head-Gordon, M.; Kochi, J. K. Intermolecular $\pi$-to-$\pi$ Bonding between Stacked Aromatic Dyads. Experimental and Theoretical Binding Energies and Near-IR Optical Transitions for Phenalenyl Radical/Radical versus Radical/Cation Dimerizations. *J. Am. Chem. Soc.* **2004**, *126*, 13850–13858.

(136) Patrascu, B.; Lete, C.; Popescu, C.; Matache, M.; Paun, A.; Madalan, A.; Ionitaa, P. Synthesis and Spectral Comparison of Electronic and Molecular Properties of Some Hydrazines and Hydrazyl Free Radicals. *Arkivoc* **2020**, *2020*, 1–10.

(137) Miura, Y.; Tanaka, A.; Hirotsu, K. ESR Studies of Nitrogen-Centered Free Radicals. 40. Exceptionally Persistent Nitrogen-Centered Free Radicals. Preparation, Isolation, and Molecular Structure of N-(Arylthio)-2,4, 6-Triphenylanilino Radicals. *J. Org. Chem.* **1991**, *56*, 6638–6643.

(138) Miura, Y.; Yamamoto, A.; Katsura, Y.; Kinoshita, M.; Sato, S.; Tamura, C. ESR Studies of Nitrogen-Centered Free Radicals. 17. [(4-Nitrophenyl)Thio](2,4, 6-Tri-Tert-Butylphenyl)Aminyl: Its Preparation, Isolation, and Molecular Structure. *J. Org. Chem.* **1982**, *47*, 2618–2622.

(139) Miura, Y.; Yamamoto, A.; Katsura, Y.; Kinoshita, M. ESR Study of Persistent Thioaminyls, N-(Arylthio)-3,5-Di-Tert-Butylphenylaminyls. *J. Org. Chem.* **1980**, *45*, 3875–3880.

(140) Miura, Y.; Tomimura, T. First Isolation of *N*-Alkoxyaminyl Radicals. *Chem. Commun.* **2001**, 627–628.

(141) Fabian, J.; Decker, D.; Mayer, R. Formation and Properties of *N*-Arylthioaminyls. *Zeitschrift fur Chemie* **1988**, *28*, 325–326.

(142) Levin, P. P.; Kokrashvili, T. A.; Kuz'min, V. A. Effect of Solvent and Substituents on Electron and Hydrogen Atom Transfer in Quenching of Quinone Triplets by Secondary Aromatic Amines. *Bulletin of the Academy of Sciences of the USSR, Division of Chemical Science* **1983**, *32*, 251–257.

(143) Miura, Y.; Tomimura, T.; Teki, Y. Heterocycle-Substituted Stable Thioaminyl Radicals: Isolation, ESR Spectra, and Magnetic Properties1. *J. Org. Chem.* **2000**, *65*, 7889–7895.

(144) Ionita, G.; Căproiu, M. T.; Meghea, A.; Maior, O.; Rovinaru, M.; Ioniță, P. Synthesis Based on 9-Amino-N-Picrylcarbazyl. *Pol. J. Chem.* **1999**, *73*, 1177–1183.

(145) Symons, M. C. R.; Pena-Nuñez, A. S. Solvation of Nitroxides. *J. Chem. Soc., Faraday Trans. 1* **1985**, *81*, 2421–2435.

(146) Imino- and Bis-Imino-Pyridines With N-Ter-Butyl-N-Aminoxyl Group: Synthesis, Oxidation and Use As Ligand Towards $M_2^+$ (Mn, Ni, Zn) and $Gd_3^+$. *J. Organomet. Chem.* **2005**, *690*, 197–210.

(147) Golubev, V. A.; Sen', V. D. Mechanism of Autoreduction of Bis(4-Methoxyphenyl)-Oxoammonium Perchlorate in Aqueous Alkali. *Russ. J. Org. Chem.* **2011**, *47*, 1313–1317.

(148) Oka, H.; Tamura, T.; Miura, Y.; Teki, Y. Synthesis and Magnetic Behaviour of Poly(1,3-Phenylene)-Based Polyradical Carrying N-Tert-Butylaminoxyl Radicals. *J. Mater. Chem.* **1999**, *9*, 1227–1232.

(149) Sueishi, Y.; Yoshioka, C.; Takemoto, K.; Kotake, Y. An Optical Spectroscopic Study on Carbon–And Oxygen-Centered Free Radical Adducts Trapped by a Bi-Functional Nitrone Spin Trap. *Zeitschrift fur Physikalische Chemie* **2002**, *216*, 1353 – 1360.

(150) Sasaki, S.; Kato, K.; Yoshifuji, M. Synthesis and Redox Properties of Crowded Triarylphosphines Carrying a Nitroxide Radical and Related Compounds. *Bull. Chem. Soc. Jpn.* **2007**, *80*, 1791–1798.

(151) Kigoshi, M.; Sato, K.; Niki, E. Oxidation of Lipids Induced by Dioctadecyl Hyponitrite and Di-*t*-Butyl Hyponitrite in Organic Solution and in Aqueous Dispersions. Effects of Reaction Medium and Size of Radicals on Efficiency of Chain Initiation. *Bull. Chem. Soc. Jpn.* **1993**, *66*, 2954–2959.

(152) Grabner, G.; Koehler, G.; Marconi, G.; Monti, S.; Venuti, E. Photophysical Properties of Methylated Phenols in Nonpolar Solvents. *J. Phys. Chem.* **1990**, *94*, 3609–3613.

(153) Modarelli, D. A.; Rossitto, F. C.; Lahti, P. M. Convenient Unimolecular Sources of Aryloxyl Radicals I – Aryloxyoxalyl Chlorides. *Tetrahedron Lett.* **1989**, *30*, 4473–4476.

(154) Ouchi, A.; Nagaoka, S.-I.; Mukai, K. Tunneling Effect in Regeneration Reaction of Vitamin E by Ubiquinol. *J. Phys. Chem. B* **2010**, *114*, 6601–6607.

(155) Roginskii, V. A.; Dubinskii, V. Z.; Miller, V. B. Dissociation of 4-Tert-Butoxy-2, 6-Di-Tertbutylphenoxyl and Antioxid Ative Activity of Phenols with Alkoky Substituents. *Bulletin of the Academy of Sciences of the USSR, Division of Chemical Science* **1981**, *30*, 2341–2344.

(156) Orio, M.; Jarjayes, O.; Baptiste, B.; Philouze, C.; Duboc, C.; Mathias, J.-L.; Benisvy, L.; Thomas, F. Geometric and Electronic Structures of Phenoxyl Radicals Hydrogen Bonded to Neutral and Cationic Partners. *Chem. Eur. J.* **2012**, *18*, 5416–5429.

(157) Rausch, R.; Schmidt, D.; Bialas, D.; Krummenacher, I.; Braunschweig, H.; Würthner, F. Stable Organic (Bi)Radicals by Delocalization of Spin Density into the Electron-Poor Chromophore Core of Isoindigo. *Chem. Eur. J.* **2018**, *24*, 3420–3424.

(158) Mitsuoka, M.; Sakamaki, D.; Fujiwara, H. Tetrathiafulvalene-Inserted Diphenoquinone: Synthesis, Structure, and Dynamic Redox Property. *Chem. Eur. J.* **2020**, *26*, 14144–14151.

(159) Tibshirani, R. Regression Shrinkage and Selection via the Lasso. *J. R. Stat. Soc. Series B Stat. Methodol.* **1996**, *58*, 267–288.

(160) Ho, T. K. Random Decision Forests. *Proceedings of 3rd International Conference on Document Analysis and Recognition* **1995**, *1*, 278–282.

(161) Friedman, J. H. Stochastic Gradient Boosting. *Comput. Stat. Data Anal.* **2002**, *38*, 367–378.

(162) Chen, T.; Guestrin, C. XgBoost: A Scalable Tree Boosting System. *Proceedings of the 22nd ACM SIGKDD International Conference on Knowledge Discovery and Data Mining* **2016**, 785–794.

(163) Ke, G.; Meng, Q.; Finley, T.; Wang, T.; Chen, W.; Ma, W.; Ye, Q.; Liu, T.-Y. LightGBM: A Highly Efficient Gradient Boosting Decision Tree. *Adv. Neural Inf. Process. Syst.* **2017**, *30*, 3146–3154.

(164) Vovk, V. Kernel Ridge Regression. In *Empirical Inference: Festschrift in Honor of*

*Vladimir N. Vapnik*; Schölkopf, B., Luo, Z., Vovk, V., Eds.; Springer Berlin Heidelberg: Berlin, Heidelberg, 2013; pp 105–116.

(165) Cortes, C.; Vapnik, V. Support-Vector Networks. *Mach. Learn.* **1995**, *20*, 273–297.

(166) Balabin, R. M.; Lomakina, E. I. Support Vector Machine Regression (LS-SVM)—An Alternative to Artificial Neural Networks (ANNs) for the Analysis of Quantum Chemistry Data? *Phys. Chem. Chem. Phys.* **2011**, *13*, 11710–11718.

(167) Kamath, A.; Vargas-Hern/'andez, R. A.; Krems, R. V.; Carrington, T.; Manzhos, S. Neural Networks vs Gaussian Process Regression for Representing Potential Energy Surfaces: A Comparative Study of Fit Quality and Vibrational Spectrum Accuracy. *J. Chem. Phys.* **2018**, *148*, 241702.

(168) Zhou, Y.; Wu, J.; Chen, S.; Chen, G. Toward the Exact Exchange–Correlation Potential: A Three-Dimensional Convolutional Neural Network Construct. *J. Phys. Chem. Lett.* **2019**, *10*, 7264–7269.

(169) Sun, W.; Zheng, Y.; Yang, K.; Zhang, Q.; Shah, A. A.; Wu, Z.; Sun, Y.; Feng, L.; Chen, D.; Xiao, Z. et al. Machine Learning-Assisted Molecular Design and Efficiency Prediction for High-Performance Organic Photovoltaic Materials. *Sci. Adv.* **2019**, *5*, eaay4275.

(170) Meftahi, N.; Klymenko, M.; Christofferson, A. J.; Bach, U.; Winkler, D. A.; Russo, S. P. Machine Learning Property Prediction for Organic Photovoltaic Devices. *Npj Comput. Mater.* **2020**, *6*, 166.

(171) Mahmood, A.; Wang, J.-L. Machine Learning for High Performance Organic Solar Cells: Current Scenario and Future Prospects. *Energy Environ. Sci.* **2021**, *14*, 90–105.

(172) Jiang, D.; Wu, Z.; Hsieh, C.-Y.; Chen, G.; Liao, B.; Wang, Z.; Shen, C.; Cao, D.; Wu, J.; Hou, T. Could Graph Neural Networks Learn Better Molecular Representation for Drug Discovery? A Comparison Study of Descriptor-Based and Graph-Based Models. *J. Cheminformatics* **2021**, *13*, 1–23.

(173) Fabregat, R.; Fabrizio, A.; Engel, E. A.; Meyer, B.; Juraskova, V.; Ceriotti, M.; Corminboeuf, C. Local Kernel Regression and Neural Network Approaches to the Conformational Landscapes of Oligopeptides. *J. Chem. Theory Comput.* **2022**, *18*, 1467–1479.

(174) Efron, B.; Hastie, T.; Johnstone, I.; Tibshirani, R. Least Angle Regression. *Ann. Statist.* **2004**, *32*, 407–499.

(175) Ju, C.-W.; French, E. J.; Geva, N.; Kohn, A. W.; Lin, Z. Stacked Ensemble Machine Learning for Range-Separation Parameters. `https://github.com/Lin-Group-at-UMass/ML-wPBE`, 2022.

(176) Epifanovsky, E.; Gilbert, A. T. B.; Feng, X.; Lee, J.; Mao, Y.; Mardirossian, N.; Pokhilko, P.; White, A. F.; Coons, M. P.; Dempwolff, A. L. et al. Software for the Frontiers of Quantum Chemistry: An Overview of Developments in the Q-Chem 5 Package. *J. Chem. Phys.* **2021**, *155*, 084801.

(177) Landrum, G. RDKit: Open-Source Cheminformatics Software. 2016; `https://github.com/rdkit/rdkit/releases/tag/Release_2016_09_4`.

(178) Hohenberg, P.; Kohn, W. Inhomogeneous Electron Gas. *Phys. Rev.* **1964**, *136*, B864–B871.

(179) Kohn, W.; Sham, L. J. Self-Consistent Equations Including Exchange and Correlation Effects. *Phys. Rev.* **1965**, *140*, A1133–A1138.

(180) Runge, E.; Gross, E. K. U. Density-Functional Theory for Time-Dependent Systems. *Phys. Rev. Lett.* **1984**, *52*, 997–1000.

(181) Petersilka, M.; Gossmann, U. J.; Gross, E. K. U. Excitation Energies from Time-Dependent Density-Functional Theory. *Phys. Rev. Lett.* **1996**, *76*, 1212–1215.

(182) van Leeuwen, R. Causality and Symmetry in Time-Dependent Density-Functional Theory. *Phys. Rev. Lett.* **1998**, *80*, 1280–1283.

(183) Kiefer, J. Sequential Minimax Search for a Maximum. *Proc. Am. Math. Soc.* **1953**, *4*, 502–506.

(184) Cossi, M.; Barone, V.; Cammi, R.; Tomasi, J. *Ab Initio* Study of Solvated Molecules: A New Implementation of the Polarizable Continuum Model. *Chem. Phys. Lett.* **1996**, *255*, 327–335.

(185) Glem, R. C.; Bender, A.; Arnby, C. H.; Carlsson, L.; Boyer, S.; Smith, J. Circular Fingerprints: Flexible Molecular Descriptors with Applications from Physical Chemistry to ADME. *IDrugs* **2006**, *9*, 199–204.

(186) Yap, C. W. PaDEL-Descriptor: An Open Source Software to Calculate Molecular Descriptors and Fingerprints. *J. Comput. Chem.* **2011**, *32*, 1466–1474.

(187) Hinton, G. E.; Roweis, S. Stochastic Neighbor Embedding. *Advances in Neural Information Processing Systems* **2002**, *15*.

(188) Cheng, L.; Sun, J.; Miller, T. F. I. Accurate Molecular-Orbital-Based Machine Learning Energies via Unsupervised Clustering of Chemical Space. *J. Chem. Theory Comput.* **2022**, *18*, 4826–4835.

(189) Townsend, J.; Micucci, C. P.; Hymel, J. H.; Maroulas, V.; Vogiatzis, K. D. Representation of Molecular Structures with Persistent Homology for Machine Learning Applications in Chemistry. *Nat. Comm.* **2020**, *11*, 3230.

(190) Janet, J. P.; Duan, C.; Nandy, A.; Liu, F.; Kulik, H. J. Navigating Transition-Metal Chemical Space: Artificial Intelligence for First-Principles Design. *Acc. Chem. Res.* **2021**, *54*, 532–545.

(191) Janet, J. P.; Kulik, H. J. Resolving Transition Metal Chemical Space: Feature Selection for Machine Learning and Structure–Property Relationships. *J. Phys. Chem. A* **2017**, *121*, 8939–8954.

(192) Naveja, J. J.; Medina-Franco, J. L. Finding Constellations in Chemical Space Through Core Analysis. *Front. Chem.* **2019**, *7*, 510.

(193) Cohen, A. J.; Mori-Sánchez, P.; Yang, W. Challenges for Density Functional Theory. *Chem. Rev.* **2012**, *112*, 289–320.

(194) Reuther, A.; Kepner, J.; Byun, C.; Samsi, S.; Arcand, W.; Bestor, D.; Bergeron, B.; Gadepally, V.; Houle, M.; Hubbell, M. et al. Interactive Supercomputing on 40,000 Cores for Machine Learning and Data Analysis. *2018 IEEE High Performance Extreme Computing Conference (HPEC)* **2018**, 1–6.

# TOC Graphic